Slovak University of Technology in Bratislava
Faculty of Civil Engineering

MSc. Konan A. Allaly

Dissertation Thesis Abstract

Image processing methods for quantitative analysis of aorta vasculitis in nuclear medicine

to obtain the Academic Title of *Philosophiae Doctor (PhD.)*
in the doctorate degree study programme
9.1.9 Applied Mathematics
full-time study

Bratislava 2026

The dissertation thesis has been prepared at the Department of Mathematics and Descriptive Geometry, Faculty of Civil Engineering, Slovak University of Technology in Bratislava

Submitter: MSc. Konan A. Allaly
Department of Mathematics and
Descriptive Geometry
Faculty of Civil Engineering, STU, Bratislava

Supervisor: prof. RNDr. Karol Mikula, DrSc.
Department of Mathematics and
Descriptive Geometry
Faculty of Civil Engineering, STU, Bratislava

Dissertation Thesis Abstract was sent: .....

Dissertation Thesis Defense will be held on ..... at ..... am/pm at the Department of Mathematics and Descriptive Geometry, Faculty of Civil Engineering, Slovak University of Technology in Bratislava, Radlinského 11, 810 05 Bratislava.

prof. Ing. Stanislav Unčík, PhD.
Dean of the Faculty of Civil Engineering

Abstract

This dissertation thesis proposes an image processing solution for nuclear medicine, particularly for the diagnosis of large vessel vasculitis using FDG-PET/CT imaging. Vasculitis is an inflammatory disease affecting blood vessels, and FDG is a glucose analog that allows the visualization of metabolically active cells, such as inflammatory cells, on PET. We propose a segmentation of the aorta, as a large vessel, that combines the minimal path approach, 3D curve evolution, and the GSUBSURF method. Segmentation is used to define precise regions of interest in the aorta to evaluate disease activity, represented by FDG concentration in the PET image. For an objective evaluation, we also segmented the liver and used it as a reference. Additional approaches are proposed to the routine approach to define regions of interest in the aorta. Instead of focusing only on the most affected region, we propose using the aorta's anatomical segments as regions of interest. We also propose to use the aorta centerline and segmentation to define one region of interest for each centerline point. These methods enable assessment of the overall distribution of aortic inflammation, including precise identification of the most affected aortic region. The framework shows promising results, accurately identifying affected regions and aligning with expert diagnoses. It enabled us to demonstrate a 42.33% reduction in inflammation in a patient with vasculitis, as shown by pre- and post-treatment FDG-PET/CT imaging.

Abstrakt

Táto dizertačná práca navrhuje riešenia na báze spracovania obrazu pre nukleárnu medicínu, konkrétne pre diagnostiku vaskulitídy veľkých ciev pomocou FDG-PET/CT obrazov. Vaskulitída je zápalové ochorenie postihujúce cievy a FDG je analóg glukózy, ktorý umožňuje vizualizáciu metabolicky aktívnych buniek, ako sú zápalové bunky, na PET snímkach. Navrhujeme segmentáciu aorty, ako veľkej cievy, ktorá kombinuje prístup minimálnej cesty, evolúciu 3D krivky a metódu GSUBSURF. Segmentácia sa používa na definovanie presných oblastí záujmu v aorte na hodnotenie aktivity ochorenia, reprezentovanej koncentráciou FDG v PET obraze. Pre objektívne hodnotenie sme taktiež segmentovali pečeň a použili ju ako referenčný orgán. Tradičný prístup definovania oblastí záujmu v aorte je rozšírený o nové prístupy. Namiesto zamerania sa iba na najviac postihnutú oblasť navrhujeme využiť anatomické segmenty aorty ako oblasti záujmu. Taktiež navrhujeme použiť stredovú líniu aorty a segmentáciu aorty na definovanie oblasti záujmu pre každý bod stredovej línie. Tieto metódy umožňujú hodnotenie celkového rozloženia aortálneho zápalu, vrátane presnej identifikácie najviac postihnutej oblasti aorty. Navrhnuté riešenie vykazuje sľubné výsledky, presne identifikuje postihnuté oblasti a je v súlade s diagnózami odborníkov. Umožnilo nám preukázať zníženie zápalu o 42,33 % u pacienta s vaskulitídou, čo bolo preukázané na snímkach FDG-PET/CT pred a po liečbe.

Contents

1 Introduction

The aorta is the main artery of the human body, carrying oxygen-rich blood from the heart to the rest of the body. Aortic aneurysm and acute aortic syndromes are the most common serious diseases affecting the aorta [18]. Segmentation of the aorta is crucial for various medical image analyses, including the diagnosis and treatment of large-vessel vasculitis (LVV). In this work, we focus on the diagnosis of LVV using FDG-PET/CT nuclear medicine imaging, in which non-enhanced CT is combined with PET to better localize organs without compromising PET image quality. LVV is an inflammatory disease that affects the aorta and can lead to severe complications such as aortic dissection if left untreated. PET imaging uses radioactive substances (radiotracers) to visualize metabolic activity within the body and detect abnormalities. FDG is a glucose analog wich show high concentration in metabolically active cells. Increased FDG uptake in the aorta wall is characteristic of vasculitis in PET [6]. FDG-PET images are interpreted using visual or quantitative approaches; the latter requires manual definition of regions of interest (ROIs) in the affected region. The visual analysis is subject to interobserver bias due to simultaneous contrast, in which the interpretation of the activity depends on the surroundings. The manual ROI delineation is laborious and difficult to reproduce. Therefore, there is a real need to design a fast, precise, and reproducible approach to define ROIs for interpreting FDG-PET image data. Some works have addressed these questions before us [15]. The proposed segmentation approaches include thresholding and region growing directly applied to the PET image data. These approaches suffer from

poor PET resolution and recurrent noise. Due to the low resolution of PET images, this work focuses on accurate aortic segmentation from CT data, and the segmentations are aligned (registered) with the PET image to define precise ROIs.

Image segmentation is the process of dividing a given image into regions based on pixel values or locations. Segmentation from CT image data is a complex task due to weak or missing edges and noise. Thresholding, region growing, and deformable models are widely used image segmentation approaches, as well machine learning and deep-learning based approaches [1, 4, 14, 10, 7, 8, 20, 25, 30, 29, 26]. Our aorta and liver segmentation approaches combine the minimal path approach, 3D curve evolution, the GSUBSURF model, thresholding, connected-component labeling, and morphological operations.

We propose a quantitative analysis that compares the aorta's maximum standardized uptake value ($\mathrm{SUV}_{\mathrm{max}}$) within the aorta(ROI) with the mean SUV ($\mathrm{SUV}_{\mathrm{mean}}$) within a reference organ, in our case, the liver. In addition to the clinical routine approach that extracts the region of interest from the most affected region of the aorta, we propose two alternative approaches. The first approach suggests splitting the aorta into anatomical segments (ascending aorta, aortic arch, descending thoracic aorta, and abdominal aorta) and considering each segment as an ROI. The second approach suggests using the aorta centerline and segmentation to define one aorta(ROI) for each centerline point. These approaches yield a distribution of $\mathrm{SUV}_{\mathrm{ratio}}$ along the aorta.

2 Segmentation of the aorta

The proposed aorta segmentation approach comprises three steps. First, we use the minimal path approach [11] to extract a path within the aorta. Usually, the minimal path approach does not lead to a centered path [11, 13]. Therefore, we move the extracted path to the aorta centerline by a 3D Lagrangian curve evolution model [23]. Finally, the aorta centerline is used to construct the initial condition for the GSUBSURF model [22]. Applying the GSUBSURF model with this initial condition yields accurate aorta segmentation. An additional algorithm, based on analysis of the unit tangent vector along the aorta centerline, is proposed to split the segmented aorta into anatomical segments.

2.1 Path extraction within the aorta

The minimal path approach was introduced in [11] as a global minimization formulation of a "modified" snake [14] energy between two endpoints. Considering a parametric curve $\Gamma(s) : \Omega \to \mathbb{R}^3$, the energy of the model is given by $E : \mathcal{A}_{p_s,p_f} \to \mathbb{R}$

$$E(\Gamma) = \int_\Omega \omega + P(\Gamma(s))ds = \int_\Omega \tilde{P}(\Gamma(s))ds \tag{1}$$

where s is the arc-lenght parameter, $\tilde{P} = \omega + P$ is the potential defined from the image, $\mathcal{A}_{p_s,p_f}$ is the space of all curves connecting the starting point p_s and a final point p_f. The parameter $\omega > 0$ is used to control the smoothness of the curve. At each point p in the image domain, and for $\tilde{P} > 0$, the minimal action U_{p_s} corresponds to the minimal energy

integrated along a path that starts at p_s and ends at p

$$U_{p_s}(p) = \inf_{\mathcal{A}_{p_s,p}} \left(\int_{\Omega} \tilde{P} ds \right) = \inf_{\mathcal{A}_{p_s,p}} E(\Gamma) \tag{2}$$

The authors of [11] showed that U_{p_s} has one global minimum located at the starting point p_s and U_{p_s} increases from p_s to the entire domain in a front propagation manner. Therefore, U_{p_s} satisfies the Eikonal equation

$$||\nabla U_{p_s}|| = \tilde{P}, \qquad U_{p_s}(p_s) = 0. \tag{3}$$

In this work, similarly to [11], we employ the *Fast Marching* method [27] to compute U_{p_s}. The minimal path Γ_{p_s,p_f} between any point p_f and the starting point p_s can be found by back-propagation on the map U_{p_s}. To find Γ_{p_s,p_f}, the authors in [13] suggest the *Steepest Descent Gradient* method.

The definition of the potential function depends on the application. An effective potential exhibits strong contrast between the regions of interest, their boundaries, and the surrounding background. For our application, we propose the following potential function:

$$\tilde{P}(p) = \left(\omega + \frac{|\tilde{I}(p_s) - I(p)|}{\max\limits_{q \in \mathcal{I}} (|\tilde{I}(p_s) - I(q)|)} \right) \frac{1}{1 + d(p)}, \ \forall p \in \mathcal{I} \tag{4}$$

where $\mathcal{I} \subset \mathbb{R}^d$, $d = 2, 3$, is the image domain, $\tilde{I}(p_s)$ is the mean image intensity value in a spherical volume centered at the starting point p_s, and $I(p)$ is the image intensity at point $p \in \mathcal{I}$. The term in parentheses emphasizes voxels that differ from p_s. The second term is a function of d, which is the distance map computed on the edge image (see [3] for details). In the best scenario, this potential yields a centered path.

Due to the elongated and variable shape of the aorta, it may happen that the extracted path does not always lie within the aorta. This situation occurs more often when the input image has low contrast. To overcome this problem, we employ the minimal path approach with keypoints detection [5]. The idea is to update the starting point during the front propagation, denoted as a keypoint within the aorta, before the front reaches the final point. The extracted path is then a set of small paths connecting the detected keypoints.

2.1.1 Results and discussion

In this section, we present the results of path extraction within the aorta. Fig. 1 illustrates extracted paths using our proposed potential function $\tilde{P}$ (4) for two different patients.

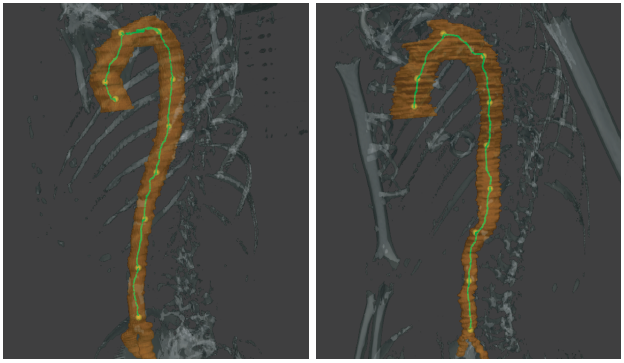

Figure 1: Extracted paths for two different patients using the minimal path approach with keypoints detection. The yellow dots are endpoints, and the found keypoints. The aorta is segmented manually only for visualization purposes.

2.2 Path centering - aorta centerline extraction

Due to the low contrast in the input CT image data, some key-points may be located near the aorta edges, resulting in a path that is not globally centered. In this section, we use a 3D Lagrangian curve evolution model, presented in [23], to move the extracted path to the aorta centerline.

Let $\Gamma : [0,1] \rightarrow \mathbb{R}^3$, $\Gamma = \{\mathbf{r}(t,u), u \in [0,1]\}$ be an open curve depending on time t and let $\mathbf{r}(t,u) = (x(t,u), y(t,u), z(t,u))$ be a position vector of the curve Γ for the parameter u in time t. The discretized curves are represented by a set of 3D points $\mathbf{r}_i^n = (x_i^n, y_i^n, z_i^n)$, where $i = 0, ..., m$, is the grid points number, and n represents the time step. The curve evolution model is based on the solution of the following partial differential equation [23]

$$\partial_t \mathbf{r} - \alpha \partial_s \mathbf{r} = \mu \mathbf{N_v} + \epsilon \partial_{ss} \mathbf{r} \tag{5}$$

where $\mathbf{N_v} = \mathbf{v} - (\mathbf{T} \cdot \mathbf{v})\mathbf{T}$ is the projection of the vector field $\mathbf{v}$ to the curve's normal plane, $k\mathbf{N} = \partial_{ss}\mathbf{r}$ is the curvature vector, α the tangential velocity, $\mathbf{T} = \partial_s \mathbf{r}$ the unit tangent vector to the curve, μ and ϵ are parameters. The Dirichlet boundary condition is applied to the model, i.e., the first and last points are fixed.

The evolution of a given is governed by a vector field. For a given tubular structure, the distance to the edge inside the structure has a ridge along the centerline, and the gradient of that distance function points towards the ridge [23]. Therefore, for path centering purposes, the vector field is defined by $\mathbf{v} = \nabla d$, where d is the distance function inside the structure of interest. A suitable tangential velocity α is presented and described in [23].

The approximation of (5) by a flowing semi-implicit finite volume scheme leads to the following numerical scheme [23, 24]

$$\mathcal{A}_i^n\ \mathbf{r}_{i-1}^{n+1} + \mathcal{B}_i^n\ \mathbf{r}_i^{n+1} + \mathcal{C}_i^n\ \mathbf{r}_{i+1}^{n+1} = \mathcal{F}_i^n \tag{6}$$

where the coefficients $\mathcal{A}_i^n$, $\mathcal{B}_i^n$, $\mathcal{C}_i^n$, and $\mathcal{F}_i^n$ are given by

$$\mathcal{A}_i^n = -\frac{\varepsilon}{h_i^n} - \frac{1}{2} b_{i-\frac{1}{2}}^{in}, \qquad \mathcal{C}_i^n = -\frac{\varepsilon}{h_{i+1}^n} - \frac{1}{2} b_{i+\frac{1}{2}}^{in} \tag{7}$$

$$\mathcal{B}_i^n = \frac{h_i^n + h_{i+1}^n}{2\tau} - (\mathcal{A}_i^n + \mathcal{C}_i^n) \tag{8}$$

$$\mathcal{F}_i^n = \frac{h_i^n + h_{i+1}^n}{2\tau}\mathbf{r}_i^n + \mu(\mathbf{N_v})_i^n \frac{h_i^n + h_{i+1}^n}{2} - \frac{1}{2} b_{i+\frac{1}{2}}^{out}(\mathbf{r}_i^n - \mathbf{r}_{i+1}^n) - \frac{1}{2} b_{i-\frac{1}{2}}^{out}(\mathbf{r}_i^n - \mathbf{r}_{i-1}^n). \tag{9}$$

The equation (6) represents three tridiagonal systems for the x, y, and z coordinates of the grid points $\mathbf{r}_i^n$, which represent the evolving curve points and can be solved using the Thomas algorithm.

2.2.1 Results and discussion

In this section, we present the results of the 3D curve evolution for path centering. Fig. 2 shows the resulting aorta centerline for 2 different patients. The velocity vector field $\mathbf{v}$ is constructed with the edge image since we do not have the aorta segmentation at this step (see [2] for details about the edge image).

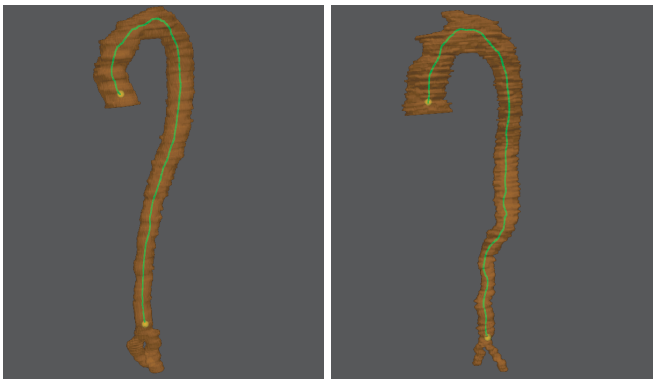

Figure 2: Centered paths (aorta centerline for two different patients) obtained by evolving the initial paths under the velocity field within the aorta.

2.3 Generalized Subjective Surface model

Let $I : \mathcal{I} \subset \mathbb{R}^3 \to \mathbb{R}$ represents the image to be segmented. The image is filtered by the geodesic mean curvature flow filtering [16]. The GSUBSURF model consists of defining an initial condition and letting it evolve according to the following advection-diffusion partial differential equation

$$u_t - w_{ad}\nabla g \cdot \nabla u - w_{dif}|\nabla u| g \nabla \cdot \left(\frac{\nabla u}{|\nabla u|}\right) = 0 \tag{10}$$

where $u(X,t)$ is the segmentation function, $g(s) = \frac{1}{1+Ks^2}$ is an edge detector function, $K > 0$ is used to control the edge detection sensibility, and $s = |\nabla I|$. The parameters $w_{ad}, w_{dif} \in \mathbb{R}$ are used to control the advection and diffusion parts of the model [22]. The advection term moves the initial curve toward the edges, while the diffusion term

handles the changes in the curve shape during evolution. We solve the problem in the domain $\mathcal{I} \times [0, T]$ and use the following boundary and initial conditions

$$u(X,t) = 0, \ \forall X \in \partial\mathcal{I}, \qquad \text{and} \qquad u(X,0) = u^0(X).$$

The initial segmentation function is typically defined by a peak located approximately at the center of gravity of the object to be segmented [22]. Therefore, we use the aorta's approximate centerline extracted in the section 2.1 to construct the initial condition

$$u^0(X) = \frac{1}{1 + d(X)}, \quad X \in \mathcal{I} \subset \mathbb{R}^3, \tag{11}$$

where $d(X)$ is minimal distance between X and the input path Γ. We use a semi-implicit finite volume scheme [21, 22] to discretize (10). We denote p the current finite volume and $N(p) = \{e, w, n, s, t, b\}$ the set of its neighbors q. Let $m(p)$ denote the measure of the finite volume p, $m(e_{pq})$ the area of a common boundary e_{pq}, and $m(\sigma_{pq})$ the distance between the centers of p and q. The numerical scheme is written as follows

$$\frac{u_p^{n+1} - u_p^n}{\tau} m(p) + \sum_{q \in N(p)} min(v_{pq}, 0)(u_q^{n+1} - u_p^{n+1}) = \\ w_{dif} |\nabla u_p^n| g_p \sum_{q \in N(p)} \frac{m(e_{pq})}{m(\sigma_{pq})} \frac{u_q^{n+1} - u_p^{n+1}}{|\nabla u_{pq}^n|} \tag{12}$$

which is a linear system with unknowns u_p^{n+1}. We solve it by the successive over-relaxation (SOR) method.

The Evans-Spruck regularization [22] is used to prevent possible zero gradients in the denominators:

$$|\nabla u_{pq}^n| \approx |\nabla u_{pq}^n|_\varepsilon = \sqrt{\varepsilon^2 + |\nabla u_{pq}^n|^2}, \ \varepsilon > 0. \tag{13}$$

We use the reduced diamond-cell approximation [22] to compute the norm of the gradient $|\nabla u_{pq}^n|$ and $|\nabla I_{pq}|$. The terms g_p and $|\nabla u_p^n|_\varepsilon$ are obtained using the average value of $|\nabla I_{pq}|$ and $|\nabla u_{pq}^n|$ in neighboring finite volumes q.

2.3.1 Results and discussion

In this section, we present the results of the GSUBSURF segmentation. Fig. 3 shows the segmented aorta in a 3D view for two different patients. The segmentation is stopped when the L^2 norm between the previous and current solution is less than a given tolerance 10^{-3}.

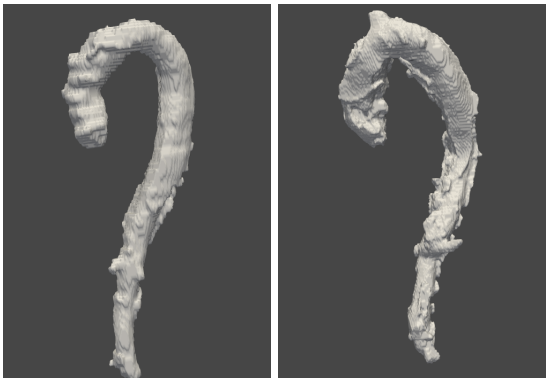

Figure 3: Segmented aortas for the two different patients, patient 4 (left) and patient 5 (right), by the GSUBSURF model.

We estimate the precision of our aorta segmentation approach using the mean Hausdorff distance, with ground truth obtained from a manual segmentation performed in *the 3D Slicer*. Table 1 shows that the segmentation results and the reference segmentations overlap, with

the maximum mean Hausdorff distance of 2.78 for patient 5, indicating the worst performance. That value corresponds to 3 voxels in the CT image and less than 1 voxel in the PET image for patient 5.

Table 1: Hausdorff distance of segmentation results

Patients	1	2	3	4	5	6
MHD	1.85	2.2	1.57	1.72	2.78	1.9

2.4 Split the aorta into segments

We propose an algorithm to split the aorta into anatomical segments. A simple model of a healthy aorta may be viewed as a sequence of connected tubular structures. The ascending aorta forms an approximately vertical tube, and the aortic arch forms a curved shape and bridges the ascending and descending aortas. The descending thoracic and abdominal aortas form a long, straight tube that runs from the chest to the abdominal area. The abdomen, located under the lungs, bridges the descending thoracic aorta and the abdominal aorta [9]. This geometric description of the aorta's shape can be obtained by analyzing the unit tangent vector along the aorta's centerline. Considering a discretized curve represented by sets of 3D points $\mathbf{r}_i^n = (x_i^n, y_i^n, z_i^n)$, where $i = 0, ..., m$, is the grid points number. The curve is parametrized by the arc length s. A geometrical interpretation of the unit tangent vector $\mathbf{T}$ along the aorta centerline is given by:

- **Ascending aorta**: positive z-coordinate of the unit tangent vector. The z-coordinate is close to 1.

- **Aortic arch**: the sign of the z-coordinate of the unit tangent vector goes from positive to negative values.
- **Descending thoracic aorta**: negative z-coordinate of the unit tangent vector. The z-coordinate is close to -1.
- **Abdominal aorta**: negative z-coordinate of the unit tangent vector. The z-coordinate is close to -1.

To obtain a reliable approximation of the unit tangent vector along the centerline, we smooth the initial centerline using the 3D curve evolution model

$$\partial_t \mathbf{r} - \alpha \partial_s \mathbf{r} = \epsilon \partial_{ss} \mathbf{r} + \lambda(\mathbf{r^0} - \mathbf{r})_{\mathbf{N}} \tag{14}$$

where $\mathbf{r}$ is the evolving curve, $\mathbf{r^0}$ is the initial curve, $k\mathbf{N} = \partial_{ss}\mathbf{r}$ the curvature vector responsible for the smoothing, and $(\mathbf{r^0} - \mathbf{r})$ the attraction vector that keeps the evolving curve as close as possible to the initial curve. The parameter ϵ weighs the curvature and λ the attraction term. The model is a 3D extension of the 2D model presented in [19]. The discretization of (14) is similar to what is done in section 2.2.

2.5 Results and discussion

In this section, we present the results of the split of the aorta into anatomical segments. Fig. 4 shows the aorta centerline and the segmented aorta for patient 1, divided into segments (portions) obtained by applying the algorithm presented in section 2.4. The segmentation in the first image was obtained using GSUBSURF. The segments (in the second image) are obtained by the intersection between the GSUBSURF segmentation and spheres defined at each centerline point and the aorta local radius.

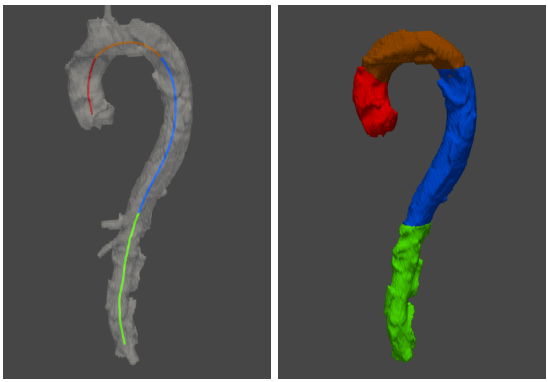

Figure 4: Patient 1 aorta centerline split into segments (left). The corresponding segmented aorta is split into segments (right). Ascending aorta (red), aortic arch (orange), descending thoracic aorta (blue), and abdominal aorta (green).

3 Segmentation of the liver

The proposed liver segmentation approach comprises four steps. First, we apply multilevel thresholding to the input image within the liver voxel values range, yielding a binary image in which the foreground voxels correspond to the liver and other structures with similar voxel intensities. In non-enhanced CT, healthy liver voxel values typically range from 40 to 60 HU [17]. However, HU values vary with scanner type and acquisition settings; therefore, we used a broader threshold range of -30 to 200 HU for our dataset to account for these variations and include unhealthy livers. In the second step, we apply connected-component labeling to identify the largest component, which contains

the liver. In the third step, we apply several times erosion to separate the liver from neighboring structures. The liver is then extracted from the binary image as the largest region using the connected-component labeling algorithm. Erosion significantly shrinks the liver; therefore, we apply the dilation, in the last step, to refine the liver shape to improve the detection of the right lobe centroid.

3.1 Results and discussion

In this section, we present the results of our liver segmentation approach. The left image of Fig. 5 shows the rough liver segmentation obtained by thresholding, connected-component labeling, and erosion. As we can see in the rough segmentation, there are holes inside the liver segmentation due to erosion. The holes may affect the identification of the liver centroid; that is why the dilation step is performed to fill the holes and improve the centroid detection (see right image on Fig. 5).

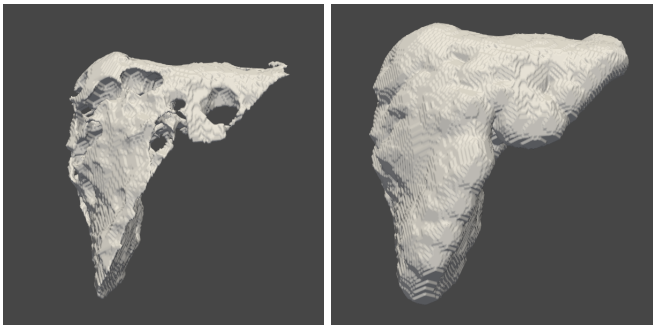

Figure 5: Segmented liver after thresholding, erosion, and connected component labeling (left). Refined segmentation (right) by dilation.

4 Diagnosis of LVV using FDG-PET/CT imaging

In this section, we present the application of the aorta and liver segmentations to the interpretation of FDG-PET images. In practice, physicians resort to quantitative analysis when visual analysis alone is insufficient to reach a conclusion [12]. Even in visual analysis, some base their conclusions on comparing aortic uptake in critical regions against a predefined threshold. This threshold is not very informative because it depends on multiple factors, including the injected FDG dose, the waiting time before the scan, and the patient's health status. For all these reasons, the quantitative approach, which compares the aorta maximum SUV ($\mathrm{SUV}_{\mathrm{max}}$) within the ROI with the mean SUV ($\mathrm{SUV}_{\mathrm{mean}}$) within a reference organ, such as the liver, is preferable [28]. Consequently, our FDG-PET interpretation is based on SUV ratio

$$\mathrm{SUV}_{\mathrm{ratio}}(\mathrm{ROI}) = \frac{\mathrm{SUV}_{\mathrm{max}}^{\mathrm{aorta(ROI)}}}{\mathrm{SUV}_{\mathrm{mean}}^{\mathrm{liver(ROI)}}}. \tag{15}$$

The liver(ROI) is defined as a spherical volume with a 3 cm diameter in the right lobe [28], which is found by computing the segmented liver centroid. For the aorta, there are multiple ways to define the aorta(ROI):

- *Entire aorta segmentation as aorta(ROI)*: the clinical routine approach suggests visually identifying the most affected aorta region and extracting a spherical volume that encompasses the aorta wall [28]. The analysis yields a single value indicating the severity of the inflammation.

- *Aorta anatomical segments as aorta(ROI)*: this approach suggests splitting the aorta into anatomical segments (ascending aorta, aortic arch, descending thoracic aorta, and abdominal aorta) and computing a single value for each segment.

- *One aorta(ROI) per centerline point*: this approach suggests using the aorta centerline and segmentation to define one aorta(ROI) per centerline point. Each centerline point is assigned the distance to the closest aorta boundary point and corresponds approximately to the aorta radius in that region. We increase this distance by two PET voxel sizes to ensure that a sphere centered at that centerline point locally encompasses the aorta boundaries, since the inflammation is located in the vessel wall (see Fig. 6). The exact segmentation around the current centerline point is then obtained by the intersection between the defined sphere and the aorta segmentation.

4.1 Results and discussions

In this section, we present the results of segmentation of the aorta and liver for the diagnosis of large vessel vasculitis using FDG-PET/CT data. Fig. 6 shows the SUV distribution in the aorta for patients 1 and 2. Based on visual analysis, one can conclude that for patient 1, the most affected regions are the descending thoracic and abdominal aortas. For patient 2, however, we observe high concentrations across all segments. In both cases, the visual analysis alone is not enough to identify the "most" affected segment.

Furthermore, when observing the distribution of SUV in the aorta

for patient 2, one might be tempted to conclude that inflammation is extensive. However, when examining the $\mathrm{SUV}_{\mathrm{ratio}}$, i.e., the comparison of the $\mathrm{SUV}_{\mathrm{max}}$ in the aorta and $\mathrm{SUV}_{\mathrm{mean}}$ in the liver it becomes clear that the maximum value of that distribution is not as high as one might think (see Table 2).

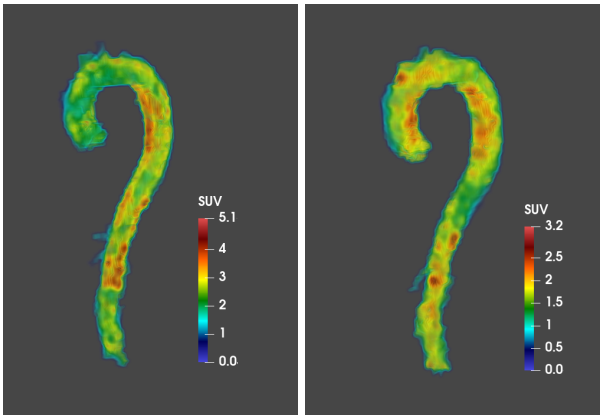

Figure 6: Aorta segmentation from PET image data for patient 1 (left) and patient 2 (right).

Table 2 shows the $\mathrm{SUV}_{\mathrm{ratio}}$ in each aorta anatomical segment for the same patient before and after treatment (patients 1 and 2). The most affected region, both before and after treatment, is the descending thoracic aorta. The quantitative approach, as we suggest, allows us to identify the most affected region of the aorta. The $\mathrm{SUV}_{\mathrm{ratio}}$ decreases significantly in all the segments after treatment, indicating a reduction in inflammation.

Table 2: Maximum SUV ratio per aorta anatomical segment for a patient before and after treatment (patients 1 and 2).

	Ascending	Arch	Descending	Abdominal
SUV_{ratio} P1	1.63	1.83	2.15	1.98
SUV_{ratio} P2	1.02	1.08	1.24	1.17

Table 3 shows the change of SUV within the liver and the aorta for the same patient before and after treatment. We note an 8.44% change in the liver ROI after treatment. This confirms the fact that considering a threshold to assess vasculitis is not objective. On the other hand, we observe a 42.33% reduction in aortic inflammation after treatment.

Table 3: SUV variation within the aorta and the liver for a patient before and after treatment

	Before	After	% variation
$SUV_{mean}^{liver(ROI)}$	2.37	2.57	+8.44
$SUV_{max}^{aorta(ROI)}$	2.15	1.24	-42.33

In Fig. 7, the x-axis corresponds to the number of points in each aorta centerline, ordered from the aortic root to the iliac bifurcation. The background colors indicate the aorta segments presented in Fig. 4. The y-axis corresponds to the calculated SUV_{ratio}. The gray line (dashed) corresponds to a ratio equal to 1. The graph before treatment indicates that vascular uptake significantly exceeds liver uptake along the aorta. This result suggests that the inflammation is very extensive and

a treatment is required. In contrast, the post-treatment graph shows lower ratios and regions with higher liver uptake. We can conclude that the treatment positively affects aortic inflammation.

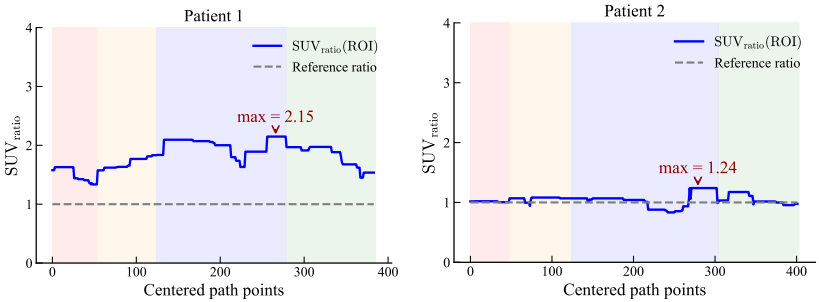

Figure 7: $\mathrm{SUV}_{\mathrm{ratio}}$ along the aorta for the same patient before treatment (left) and after treatment (right). The background colors correspond to the aorta segments presented in Fig. 4.

5 Conclusion

In this dissertation, we proposed an image-processing pipeline for diagnosing large-vessel vasculitis using FDG-PET/CT image data. It is a semi-automatic approach that segments the aorta and the liver from CT images to define precise ROIs in PET images. Disease activity is evaluated within these ROIs to assess vasculitis. Our proposed approach yields significant improvements in results by refining ROI definition and enabling easy reproducibility. The framework is built on mathematical models that have proven effective in image processing. In contrast to Machine Learning and Deep Learning approaches,

which have become increasingly popular in recent years, we propose a method that does not require a large dataset, particularly because medical images are difficult to access due to patient data protection constraints.

References

[1] R. Adams and L. Bischof, *Seeded Region Growing*, IEEE Transactions On Pattern Analysis and Machine Intelligence, 16 (1994), pp. 641–647.

[2] K. Allaly, K. Mikula, and J. Urbán, *Mathematical and numerical methods for accurate aorta segmentation from non-enhanced CT data yielding reliable identification and evaluation of large vessel vasculitis*, Tatra Mt. Math, (2026).

[3] K. Allaly and J. Urbán, *Automatic Path Extraction Inside the Aorta from CT data*, in Proceedings of the Conference Algoritmy, (2024), pp. 255–263.

[4] I. N. Bankman, ed., *Handbook of Medical Imaging: Processing and Analysis*, Academic Press, 2000.

[5] F. Benmansour and L. D. Cohen, *Fast Object Segmentation by Growing Minimal Paths from a Single Point on 2D or 3D Images*, Journal of Mathematical Imaging and Vision, 33 (2009), pp. 209–221.

[6] C. T. Berger, G. Sommer, M. Aschwanden, D. Staub, C. Rottenburger, and T. Daikeker, *The clinical benefit of*

imaging in the diagnosis and treatment of giant cell arteritis, Swiss Medical Weekly, (2018).

[7] V. Caselles, R. Kimmel, and G. Sapiro, *Geodesic Active Contours*, International Journal of Computer Vision, 22 (1997), pp. 61–79.

[8] V. Caselles, R. Kimmel, G. Sapiro, and C. Sbert, *Minimal surfaces: a geometric three dimensional segmentation approach*, Numerische Mathematik, 77 (1997), pp. 423–451.

[9] Cleaveland Clinic, *What is the anatomy of the aorta?*, 2022. (Online) Accessed: 2026-05-20.

[10] L. D. Cohen, *On active contour models and balloons*, CVGIP: Image understanding, 2 (1991), pp. 211–218.

[11] L. D. Cohen and R. Kimmel, *Global Minimum for Active Contour Models: A Minimal Path Approach*, International Journal of Computer Vision, 24 (1997), pp. 57–78.

[12] C. Dejaco, S. Ramiro, M. Bond, P. Bosch, C. Ponte, S. L. Mackie, T. A. Bley, D. Blockmans, S. B. E. C. Bolek, and al., *EULAR recommendations for the use of imaging in large vessel vasculitis in clinical practice: 2023 update*, Annals of the Rheumatic Diseases, 83 (2024), pp. 741–751.

[13] T. Deschamps and L. D. Cohen, *Fast extraction of minimal paths in 3D images and applications to virtual endoscopy*, Medical Image Analysis, 5 (2001), pp. 281–299.

[14] M. Kass, A. Witkins, and D. Terzopoulos, *Snakes: Active Contours Models*, International Journal of Computer Vision, 1 (1988), pp. 321–331.

[15] N. C. Krak, R. Boellaard, O. S. Hoekstra, J. W. R. Twisk, C. J. Hoekstra, and A. A. Lammertma, *Effects of ROI definition and reconstruction method on quantitative outcome and applicability in a response monitoring trial*, Physics in Medicine and Biology, 32 (2005), pp. 294–301.

[16] Z. Krivá, K. Mikula, N. Peyriéra, B. Rizzi, A. Sarti, and O. Stasová, *3D early embryogenesis image filtering by nonlinear partial differential equations*, Medical Image Analysis, 14 (2010), pp. 510–526.

[17] R. Lamba, J. P. McGahan, M. T. Corwin, C.-S. Li, T. Tran, J. A. Seibert, and J. M. Boone, *CT Hounsfield Numbers of Soft Tissues on Unenhanced Abdominal CT Scans: Variability Between Two Different Manufacturer's MDCT Scanners*, American Journal of Roentgenology, 203 (2014), pp. 1013–1020.

[18] D. Litmanovich, A. A. Bankier, L. Cantin, V. Raptopoulos, and P. M. Boiselle, *CT and MRI in Diseases of the Aorta*, American Journal of Roentgenology, 193 (2009), pp. 928–940.

[19] G. Lupi, K. Mikula, and S. A. Park, *Macrophages Trajectories Smoothing by Evolving Curves*, Tatra Mt. Math. Publi., 86 (2023).

[20] R. Malladi and J. A. Sethian, *Image processing via level set curvature flow*, Proc. Nat. Acad. Sci. USA, 92 (1995), pp. 7046–7050.

[21] K. Mikula, N. Peyriéras, M. Remišíková, and A. Sarti, *3D embryogenesis image segmentation by the generalized subjective surface method using the finite volume technique*, Finite Volumes for Complex Applications V: Problems and Perspectives, (2008), pp. 585–592.

[22] K. Mikula and M. Remešíková, *Finite Volume Schemes for the Generalized Subjective Surface Equation in image Segmentation*, Kybernetika, 45 (2009), pp. 646–656.

[23] K. Mikula and J. Urbán, *A new tangentially stabilized 3D curve evolution algorithm and its application in virtual colonoscopy*, Advances in Computational Mathematics, 40 (2014), pp. 819–837.

[24] K. Mikula and D. Ševčovič, *Evolution of plane curves driven by a nonlinear function of curvature and anisotropy*, SIAM J. Appl. Math., 61 (2001), pp. 1473–1501.

[25] A. Sarti and G. Citti, *Subjective Surfaces and Riemannian Mean Curvature Flow of Graphs*, in Proceedings of Algoritmy 2000, (2001), pp. 85–103.

[26] K. E. Sengun, Y. T. Cetin, M. Guzel, S. Can, and E. Bostanci, *Automatic Liver Segmentation from CT Images Using Deep Learning Algorithms: A Comparative Study*, arXiv:2101.09987, (2021).

[27] J. A. Sethian, *A fast marching level set method for monotonically advancing fronts*, in Proceedings of the National Academy of Sciences, 93 (1996), pp. 1591–1595.

[28] R. H. J. A. Slart, A. W. J. M. Glaudemans, P. Chareonthaitawee, G. Treglia, F. L. Besson, T. A. Bley, D. Blockmans, R. Boellard, J. Bucerius, J. M. Carril, and al., *FDG-PET/CT(A) Imaging in large vessel vasculitis and polymyalgia rheumatica: joint procedural recommendation of the EANM, SNMMI, and the PET Interest Group (PIG), and endorsed by the ASNC*, European Journal of Nuclear Medicine and Molecular Imaging, 45 (2018), p. 1250–1269.

[29] R. Trullo, C. Petitjean, S. Ruan, B. Dubray, D. Nie, and D. Shen, *Segmentation of organs at risk in thoracic CT images using a sharpmask architecture and conditional random fields*, 2017 IEEE 14th international symposium on biomedical imaging, (2017), pp. 1003–1006.

[30] J. Yuan, A. Pepe, J. Li, C. Gsaxner, F.-H. Zhao, K. L. Pomykalad, J. Kleesiek, A. F. Frangi, and J. Egger, *AI-based Aortic Vessel Tree Segmentation for Cardiovascular Diseases Treatment: Status Quo*, arXiv preprint arXiv, (2021).

List of author's publications

Journal Articles

- ALLALY, Konan A - URBÁN, Jozef - MIKULA, Karol. Mathematical and numerical methods for accurate aorta segmentation from non-enhanced CT data yielding reliable identification and evaluation of large vessel vasculitis. Tatra Mt. Math. Publ., 2026. ISSN 1210-3195 (print), 1338-9750 (online). DOI: 10.2478/tmmp-2026-0005. Ahead of print.

Conference Proceedings

- ALLALY, Konan A. - URBÁN, Jozef. Automatic Path Extraction Inside the Aorta from CT data. in Proceedings of the Conference Algoritmy. pp. 255–263, 2024.

- ALLALY, Konan A. - MIKULA, Karol - POVINEC, Pavol - URBÁN, Jozef. Segmentation of the aorta and application to the diagnosis of large vessel vasculitis, Proceedings of IEEE EMBC 2026, Toronto, Canada, 26–30 Jul 2026. Accepted.